AIAA JOURNAL
Vol. 44, No. 10, October 2006

Large Eddy Simulation of Transonic Flow with Shock Wave/Turbulent Boundary Layer Interaction

Christian Wollblad,[*] Lars Davidson,[†] and Lars-Erik Eriksson[‡]
Chalmers University of Technology, 412 96, Gothenburg, Sweden

DOI: 10.2514/1.20358

A large eddy simulation was made of transonic flow over a two-dimensional bump where shock wave turbulent boundary layer interaction takes place. Grid refinement and the effect of the domain width were investigated. Special care was taken to ensure physically correct inlet boundary conditions. The shock wave turbulent boundary layer interaction induces strong separation of the boundary layer and events such as bursting events in the incoming boundary layer, and creation of large flow scale structures behind the shock are detected. However, the shock features no large scale movement even though, according to several sources, the prerequisites for such movement are fulfilled.

Nomenclature

C_f = skin-friction coefficient
c_p = heat capacity, pressure coefficient in Sec. VIII
e_0 = total internal energy
f = frequency
H = shape factor
k = turbulent kinetic energy
p = pressure
q_1, q_2, q_3 = heat transfer in x, y, and z directions
P_h = power spectrum
r = recovery factor
S_{ij} = strain rate tensor
T = temperature
T_r = recovery temperature
u, v, w = velocities in x, y, and z directions; also denoted u_1, u_2 and u_3
$\langle u_i u_j \rangle$ = (resolved) Reynolds stress tensor components
γ = gas constant
$\Delta x, \Delta y, \Delta z$ = cell length, height, and width
δ_{ij} = the Kronecker delta
δ_{99} = distance from the wall where mean velocity is 99% of the freestream velocity
μ = dynamic viscosity
ν = kinematic viscosity
ρ = density
τ_{ij} = stress tensor

Subscripts

m = measured data
p = profile data
t = turbulent quantity
w = wall condition
0 = total quantity
∞ = freestream condition

Superscripts

SGS = subgrid-scale quantity
$+$ = wall friction unit
$-$ = space filtered quantity
$\sim$ = Favre-averaged quantity

I. Introduction

Shock wave turbulent boundary layer interactions (SWTBLI) have been studied for many years. These situations commonly arise in turbomachinery and aerospace applications and on the exterior of high speed aircraft. In all these cases, the shock wave boundary layer interaction can significantly change the flow and hence the physical load imposed by it. The performance of the object studied can also be significantly altered if shocks and boundary layer separations do not occur where expected.

The experimental material on SWTBLI is vast but most was produced using intrusive methods [1] and only a basic understanding of the phenomena has been achieved from older experiments [2]. There are newer techniques, of course, such as particle image velocimetry (PIV) and laser Doppler anemometry (LDA), that can give a deeper understanding [3], especially when combined with numerical simulations (see, for example, [4]). The bulk of the existing calculations are from Reynolds averaged Navier–Stokes (RANS) computations because the high computational cost has long hindered more advanced calculations. There are several reasons why RANS methods at best give only fair results. First, flows of the kind considered here include both separation and recirculation, phenomena that are difficult to capture with RANS. Second, flows with SWTBLI often feature low frequency shock motions that cannot be captured by RANS. See, for example, [1,5] for more detailed discussions. In recent years, large eddy simulations (LES) [6,7] have been made that have shown much better agreement with experiments than RANS calculations [5]. LES was thus chosen for this work.

The goal of this work is twofold. The first is to investigate the flow properties of SWTBLI in a transonic flow to help gain a deeper understanding of these flow phenomena. The second goal is to create a database for the current case. This database, together with experiments done at the Royal Institute of Technology (KTH) in Stockholm (see Sec. IV), is intended for use to develop new computational tools suitable for transonic flows. It is thus of the utmost importance that the computations are as accurate as possible.

II. Large Eddy Simulation Numerics

The solver for the Navier–Stokes equations is based on the G3D series of codes developed by L.-E. Eriksson [8]. It handles only block structured grids and solves the spatially Favre-averaged continuity, momentum, and energy equations:

Received 4 October 2005; accepted for publication 1 June 2006.

[*] Ph.D. Student, Division of Fluid Dynamics, Department of Applied Mechanics.

[†] Professor, Heat Transfer, Division of Fluid Dynamics, Department of Applied Mechanics.

[‡] Professor, Compressible Flow and Aeroacoustics, Division of Fluid Dynamics, Department of Applied Mechanics.

$$\frac{\partial \bar{\rho}}{\partial t}+\frac{\partial(\bar{\rho}\tilde{u}_j)}{\partial x_j}=0 \tag{1}$$

$$\frac{\partial \bar{\rho}\tilde{u}_i}{\partial t}+\frac{\partial(\bar{\rho}\tilde{u}_i\tilde{u}_j)}{\partial x_j}=-\frac{\partial \bar{p}}{\partial x_i}+\frac{\partial \bar{\tau}_{ij}}{\partial x_j}+\frac{\partial \tau_{ij}^{\mathrm{SGS}}}{\partial x_j} \tag{2}$$

$$\frac{\partial(\bar{\rho}\tilde{e}_0)}{\partial t}+\frac{\partial(\bar{\rho}\tilde{e}_0\tilde{u}_j)}{\partial t}=-\frac{\partial(\bar{p}\tilde{u}_j)}{\partial x_j}+\frac{\partial}{\partial x_j}\left(c_p\frac{\mu}{Pr}\frac{\partial \tilde{T}}{\partial x_j}-q_j^{\mathrm{SGS}}\right)+\frac{\partial}{\partial x_j}[\tilde{u}_i(\bar{\tau}_{ij}+\tau_{ij}^{\mathrm{SGS}})] \tag{3}$$

$\bar{\tau}_{ij}$ is the Favre-filtered viscous stress tensor:

$$\bar{\tau}_{ij}=\mu\left(2\tilde{S}_{ij}-\frac{2}{3}\tilde{S}_{mm}\delta_{ij}\right) \tag{4}$$

$\tilde{S}_{ij}$ is the Favre-filtered strain rate tensor given by

$$\tilde{S}_{ij}=\frac{1}{2}\left(\frac{\partial \tilde{u}_i}{\partial x_j}+\frac{\partial \tilde{u}_j}{\partial x_i}\right) \tag{5}$$

τ_{ij}^{SGS} is the subgrid-scale viscous tensor modeled by

$$\tau_{ij}^{\mathrm{SGS}}=\mu_t\left(2\tilde{S}_{ij}-\frac{2}{3}\tilde{S}_{mm}\delta_{ij}\right)-\frac{2}{3}\bar{\rho}k^{\mathrm{SGS}}\delta_{ij} \tag{6}$$

where μ_t and k^{SGS} depend on the subgrid model (see Sec. II.A). The subgrid heat flux q_j^{SGS} is modeled by

$$q_j^{\mathrm{SGS}}=-c_p\frac{\mu_t}{Pr_t}\frac{\partial \tilde{T}}{\partial x_j} \tag{7}$$

The filter is a box filter of grid cell size, and closure was achieved by assuming calorically perfect gas.

Some details are given here. Full details can be found in [9,10].

A. Subgrid Models and Constants

The grid study of this work is conducted using a compressible version of the Smagorinsky model [11] with a fixed filter width. In this Smagorinsky model μ_t and k^{SGS} are given by

$$\mu_t=C_R\bar{\rho}\Delta^2\sqrt{\tilde{S}_{mn}\tilde{S}_{mn}} \tag{8}$$

$$k^{\mathrm{SGS}}=C_I\Delta^2\tilde{S}_{mn}\tilde{S}_{mn} \tag{9}$$

The constants C_R and C_I were set to 0.012 and 0.0066, respectively. The dynamic viscosity is set to the constant value $1.8e^{-4}$ Pa · s (see Sec. IV.B). The filter width is chosen to be approximately equal to $(\Delta x\Delta y\Delta z)^{1/3}$ for the small, but not smallest, cells.

The Smagorinsky subgrid model is not always accurate enough, but the flaws are difficult to correct as it, for example, needs a length scale filter close to a wall and the filters commonly used do not work in separated regions. Thus a modified version of the WALE model, developed by Nicoud and Ducros [12], is used in the final calculation. The original model is developed for incompressible flow, and it thus gives only μ_t:

$$\mu_t=\bar{\rho}(C_w\Delta)^2\frac{(\mathcal{S}_{ij}^d\mathcal{S}_{ij}^d)^{3/2}}{(\tilde{S}_{ij}\tilde{S}_{ij})^{5/2}+(\mathcal{S}_{ij}^d\mathcal{S}_{ij}^d)^{5/4}} \tag{10}$$

where $C_w=0.3$ and

$$\mathcal{S}_{ij}^d=\frac{1}{2}\left(\frac{\partial \tilde{u}_i}{\partial x_l}\frac{\partial \tilde{u}_l}{\partial x_j}+\frac{\partial \tilde{u}_j}{\partial x_l}\frac{\partial \tilde{u}_l}{\partial x_i}\right)-\frac{1}{3}\frac{\partial \tilde{u}_m}{\partial x_l}\frac{\partial \tilde{u}_l}{\partial x_m}\delta_{ij} \tag{11}$$

The modification is to use the relation between μ_t and k^{SGS} in Eqs. (8) and (9) to rewrite Eq. (6) as

$$\tau_{ij}^{\mathrm{SGS}}=2\mu_t\left(\tilde{S}_{ij}-\frac{1}{3}\tilde{S}_{mm}\delta_{ij}\right)-\frac{2}{3}\frac{C_I'}{\bar{\rho}}\left(\frac{\mu_t}{\Delta}\right)^2\delta_{ij} \tag{12}$$

Using the coefficients from the Samgorinsky model, C_I' is found to be 45.8, which is used also in the modified WALE model. To make the stresses realizable, its diagonal entries were forced to be nonpositive. The dynamic viscosity is improved by implementing Sutherland's law [13], and the filter width is changed to be exactly $(\Delta x\Delta y\Delta z)^{1/3}$, i.e., to a function of the grid.

There is evidence that subgrid scale (SGS) models with only one length scale are not functional in areas with large anisotropy, for example, in separated regions [1]. However, this type of problem can be remedied if the grid is fine enough in the critical regions.

B. Flux Approximation

To evaluate the inviscid fluxes on a cell face A as shown in Fig. 1, the state vector $\boldsymbol{Q}$ is used in a plane wave assumption to obtain characteristic speeds for waves carrying entropy (λ_1), vorticity (λ_1, λ_2), and sound (λ_4, λ_5). The inviscid fluxes are approximated in space using a fourth-order central scheme, to which is added a small amount of upwinding. The coefficients of the low-dissipation upwind scheme are derived using a third-order polynomial $Q(x)$ to represent the variation of the flow state in the normal direction

$$Q(x)=A+Bx+Cx^2+Dx^3 \tag{13}$$

where x is equal to zero at face A. The face state $\boldsymbol{Q}(x=0)$ is evaluated using the interpolated value $Q(0)$ modified to include upwinding by adding the third derivative of $Q(x)$ according to

$$\begin{aligned}Q_0&=Q(0)\pm\delta\frac{\partial^3 Q}{\partial x^3}(0)=A\pm 6\delta D\\&=C_1\boldsymbol{Q}_1+C_2\boldsymbol{Q}_2+C_3\boldsymbol{Q}_3+C_4\boldsymbol{Q}_4\end{aligned} \tag{14}$$

where the coefficient δ in front of the upwind term has been chosen by numerical experiment [14] to be $1/96$ to introduce only a small amount of upwinding. The sign of the δ is for each characteristic variable in the state vector decided by the sign of the characteristic speeds λ_i. The result is the low-dissipation third-order upwind scheme used in this work, that is, low dissipation compared with a standard third-order upwind scheme, which is obtained using $\delta=1/12$. The coefficients (C_1–C_4) are

$$\begin{aligned}C_1&=-(1/12\pm\delta), &\quad C_2&=(7/12\pm 3\delta),\\C_3&=(7/12\mp 3\delta), &\quad C_4&=-(1/12\mp\delta)\end{aligned} \tag{15}$$

Again, the sign of δ is decided by the characteristic speeds.

A second-order central scheme is used to discretize the viscous fluxes.

The numerical scheme described so far cannot handle the discontinuity created at strong shocks. To prevent the calculations from diverging, extra shock handling diffusion is added. The method is developed from the ideas of Jameson et al. [15]. For the fluxes over cell face A in Fig. 1, a source term of the form

$$C_{\mathrm{PD}}\cdot\max\left(\frac{|\bar{p}_1-2\bar{p}_2+\bar{p}_3|}{\bar{p}_1+2\bar{p}_2+\bar{p}_3},\frac{|\bar{p}_2-2\bar{p}_3+\bar{p}_4|}{\bar{p}_2-2\bar{p}_3+\bar{p}_4}\right)\cdot\max(\lambda_i)\cdot(\boldsymbol{Q}_3-\boldsymbol{Q}_2) \tag{16}$$

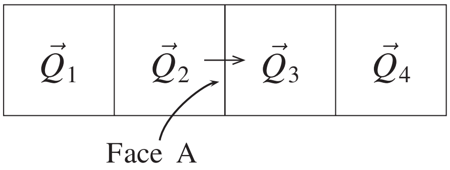

Fig. 1 Cells used to obtain the shock handling term and the inviscid fluxes.

is added. The indices on $\bar{p}$ and $\boldsymbol{Q}$ refer to Fig. 1, and the maximum of λ is taken over $i = 1, \ldots, 5$. C_{PD} is a user-defined constant that is normally set to 0.4 if shocks are expected. In this case $C_{\mathrm{PD}} = 0.05$ is enough to prevent divergence of the calculations.

III. Time Stepping

Time stepping is performed by a three-stage low-storage Runge–Kutta method [16] using a constant time step. Close to the wall, the CFL number is totally dominated by sound waves in the wall-normal direction. To enable larger time steps than allowed by an explicit method alone, a semi-implicit precondition scheme is applied close to the wall. In this scheme, the fluxes in the wall-normal direction are decoupled and a preconditioning, equivalent to making one Newton–Raphson iteration for the fluxes in the wall-normal direction, is applied before each Runge–Kutta step. The method is fully described in [17].

IV. Computational Setup

A. The Domain

The computational domain is a numerical model of a part of an experimental test rig located at the Department of Energy Technology, KTH. The experimental test section is 0.44 m long, 0.10 m wide, and 0.12 m high. There is a bump at the bottom of the test section. See [18] for greater detail about the rig. Our domain consists of this test section but has been shortened by 0.08 m, and translational periodicity was assumed in the spanwise direction for a width less than that of the test section. The width of the domain will be considered in Sec. VI. Furthermore, the ceiling has been taken away and is replaced by a symmetry plane. A 2-D picture of the domain is shown in Fig. 2. To mimic the conditions in the test rig as much as possible, the symmetry plane is lowered by one momentum loss thickness based on the inlet boundary condition so that $h = 0.1186$ m. In this way possible differences in mass displacement between measurements and calculations are prevented to a certain extent. The maximum height of the bump is 0.01048 m.

The geometry is such that, for some subsonic boundary conditions at the inlet and outlet, the flow will be accelerated over the bump and the sonic pocket that is formed will be terminated by a shock. Measurements have shown that no shock in the range of interest is so strong that it will reach up to the ceiling. Replacing the ceiling with a symmetry plane should, thus, not have any strong influence on the flowfield.

B. Flow Conditions

An LES with all conditions set as in the experimental rig would be more or less impossible owing to high computational costs. The Reynolds number based on $h/2$ and the freestream inlet conditions would then be about 10^6. The number of nodes needed for such a case is far beyond our capacity today. The Reynolds number was, therefore, decreased by increasing the viscosity by a factor of 11.25 up to $\mu = 1.8e^{-4}$ Pa · s. The boundary layer upstream of the shock is, of course, dependent on the Reynolds number. An effort to compensate for this was made by careful choice of inlet boundary conditions (see the next section). It is, however, better to carry out a well-resolved accurate LES at a reduced Reynolds number than an inaccurate LES at the original high Reynolds number.

C. Boundary Conditions

As mentioned, the upper boundary was set to be a symmetry boundary, and the spanwise boundaries were given translational periodic boundary conditions. No-slip adiabatic conditions were enforced along the wall.

From measurements in [18] it is known that there will be a shock at the back of the bump for freestream inlet boundary conditions of $M = 0.70$, $P_0 = 160.0$ kPa, and $T_0 = 303$ K and for some outlet pressure. In addition, the inlet should have a turbulent boundary layer. A boundary layer thickness of 8.95 mm was given by a measurement made by Sigfrids [19], at location $x = -0.10$ m, whereas our inlet is located at $x = -0.09$ m (see Fig. 2). The measurement was furthermore made at a higher Reynolds number due to different viscosity. The mathematical form of the inlet boundary condition was that of a nonreflective boundary condition based on flow characteristics where ρ, ρu, ρv, ρw, and ρe_0 are given as boundary values. The freestream value of these were set to $1.3766\ \mathrm{kg/m^3}$, $312\ \mathrm{N \cdot s/m^3}$, $0.0\ \mathrm{N \cdot s/m^3}$, $0.0\ \mathrm{N \cdot s/m^3}$, and $310\ \mathrm{kJ/m^3}$.

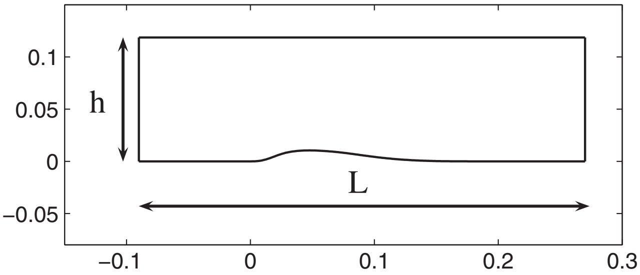

Fig. 2 2-D projection of the computational domain.

It is important in the calculations to match the experimentally obtained boundary layer thickness at the top of the bump because it determines characteristics of the SWTBLI. There are no simple tools for approximating the development of the boundary layer as it is accelerated over the bump. A theory for the incompressible turbulent boundary layer [20] was instead used to calculate the expected boundary layer thickness at the start of the bump, $x = 0.0$ m, in the test rig. Then, the δ_{99} required at $x = -0.09$ m to get the same boundary layer thickness at $x = 0.0$ m, but with the higher viscosity, was estimated to be $\delta_{99} = 8.2$ mm. Such a profile would have $Re_\tau = 615$ based on u_* and δ_{99}. The scheme of the calculation is illustrated in Fig. 3.

A profile for incompressible flow measured by Johansson and Castillo [21] was used but required rescaling. For a profile with a freestream velocity of U_∞ the following relation is valid:

$$\frac{U}{U_\infty} = f\left(\frac{xU_\infty}{\nu}, \frac{yU_\infty}{\nu}, *\right) \tag{17}$$

where f is some function describing the relation and $*$ denotes the dependence on upstream conditions. Rescaling Johansson's and Castillo's profile using this relation gave a profile with $\delta_{99} = 7.5$ mm and $Re_\tau = 632$. Both quantities are close to the desired values.

To get profiles for ρ and ρe_0, the temperature was assumed to follow the Walz distribution [13]:

$$\frac{T}{T_\infty} = \frac{T_w}{T_\infty} + \frac{T_r - T_w}{T_\infty}\left(\frac{U}{U_\infty}\right) - r\frac{\gamma - 1}{2}M_\infty^2\left(\frac{U}{U_\infty}\right)^2 \tag{18}$$

The expression

$$T_r = T_\infty + r\frac{U_\infty^2}{2c_p} = T_\infty\left(1 + r\frac{\gamma - 1}{2}M_\infty^2\right) \tag{19}$$

and $r = 0.89$ were also taken from Schlichting [13]. As the wall was set to be adiabatic, $T_w = T_r$. The pressure was assumed to be constant normal through the boundary layer, and its value was given by measurements made by Sigfrids. Combined with the ideal gas law, the desired profiles were obtained.

The fluctuations were taken from direct numerical simulation (DNS) of fully developed incompressible channel flow. The data had to be rescaled based on u_*, ν, and h_{DNS} versus δ_{99}, where h_{DNS} was half the channel height for the DNS calculation. Observe that both space and time variables needed scaling. The pressure fluctuations

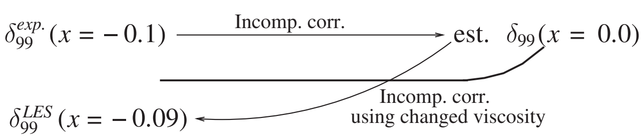

Fig. 3 Rescaling of the inlet boundary layer thickness.

were based on the dynamic pressure fluctuations from the DNS. Because the DNS was incompressible, the acoustic fluctuations were missing. They are relatively small, however, and were therefore neglected. Because fully developed channel flow has a much higher turbulent intensity in the middle of the channel than the developing boundary layer has in the outer region, the fluctuations from the DNS had to be reduced. A filter was created by comparing root mean square deviations of the DNS data with that of the measurements made by Johansson and Castillo [21]. The filter was applied to the fluctuations before they were added to the inlet profile.

In the experimental rig, the outlet pressure was used to control the strength and the position of the shock [18]. An outlet pressure of 114 kPa gave a very weak shock at $x \approx 0.05$ whereas an outlet pressure of 104 kPa gave a strong shock at $x \approx 0.07$. Measurements by Bron [18] indicated that, for an outlet pressure of 108 kPa, a maximum Mach number of 1.3 was reached right before the shock. $M = 1.3$ is generally considered the critical Mach number to attain separation for transonic flows with SWTBLI [2], and this was confirmed in Bron's experiments [18]. The problem is that the flow in the wind tunnel features large zones of separation at the side walls, and thus the flow is accelerated by 3-D effects that are neither possible nor desirable to mimic in the computational domain. The best flow configuration, which was reached for $P_{\text{out}} = 103.5$ kPa, was a shock at $x \approx 0.075$, and the maximum Mach number was 1.27 (see Sec. VI). When the same shock strength was obtained in the test rig, the shock was positioned at $x \approx 0.065$. A stronger shock could have been achieved by reducing the outlet pressure even further, but that was not done because the shock would then have moved too close to the location at which the wall curvature shifts from convex to concave.

V. Data Treatment

For each grid, a calculation was run until the average wall shear stress on the back of the bump showed no long time fluctuations. The calculations were run for approximately three flow-through times. During this time 512 instantaneous solutions with equal time spacing were saved. Tests showed that second order statistics could be calculated from only 300 samples without loss of accuracy, but 512 were chosen to fit with FFT calculations in the postprocessing.

The grids, which are structured grids, are constructed of nodes. A cell consists of eight nodes, one in each corner. The flow data are represented as averages over these cells. For each node, the values of the adjacent cells were added and the sum was divided by the number of adjacent cells. This makes the values of the interior nodes averages of eight cell values, while the values assigned to a corner node equal those of its adjacent cell.

Depending on the application, the nodal data were then either averaged in the spanwise direction or interpolated onto the cells of another grid. Flow statistics such as Reynolds stresses were calculated from data averaged in both the spanwise direction and in time. For calculation of two point correlations and frequencies, data were interpolated to a sample grid, and calculations were carried out on this grid using the cell values. The results were then averaged in the spanwise direction.

VI. Grid Studies

Resolution is always a critical issue, and in this case domain width is also critical because translational periodic boundary conditions are assumed in the spanwise direction. This section deals with those issues. Three grids are considered and are summarized in Table 1.

The first grid, grid 1, with $261 \times 121 \times 65$ nodes in the streamwise, wall-normal, and spanwise directions, respectively, was constructed to cover a width of almost 0.02 m. The domain was chosen to have this narrow width because a much wider width would have been too computationally costly. The effect of the width will be considered later in this section. The maximum stretching of this grid was 11% (which was in the wall-normal direction).

Table 1 Summary of computational grids used

Grid	Nodes	Domain width
1	$261 \times 121 \times 65$	0.0195 m
2	$306 \times 131 \times 86$	0.0195 m
3	$306 \times 131 \times 171$	0.0390 m

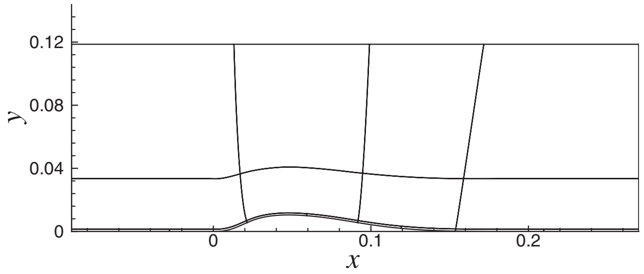

Fig. 4 Block decomposition of grid 2.

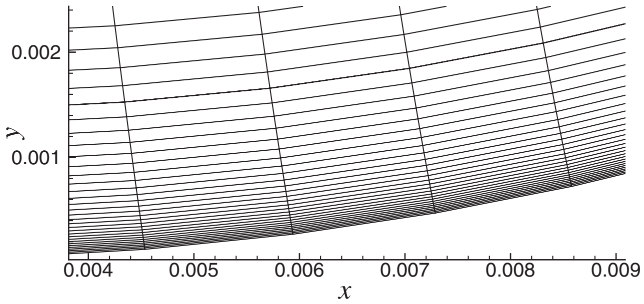

Fig. 5 Close-up of grid 2 at the foot of the bump.

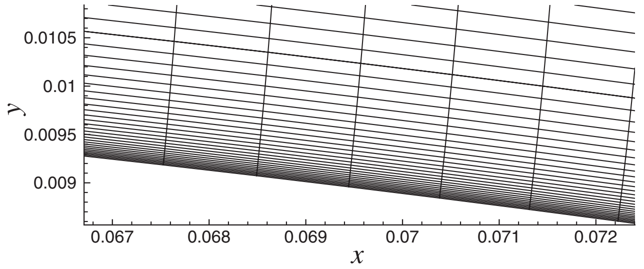

Fig. 6 Close-up of grid 2 at the shock foot position.

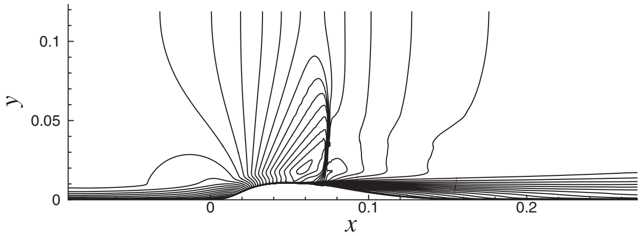

Fig. 7 Average Mach contours computed on grid 2.

Initial computations showed that the resolution in terms of Δx^+ and Δy^+ was satisfactory. In most locations Δy^+ for the first node was 0.5, and nowhere was it larger than 1. However, there was a fairly large region where Δz^+ was more than 30 with a maximum value of almost 40. A well-resolved LES should have $\Delta z^+ \approx 20$ with 40 as an absolute maximum [22]. Another grid with $306 \times 131 \times 86$ nodes spanning the same domain width was thus created. Motivation for the extra 45 nodes in the streamwise direction will be given later. A few nodes were also added in the wall-normal direction to give better stretching. Some details of this grid, grid 2, are shown in Figs. 4–6. Figure 4 shows the block decomposition of the grid, and Figs. 5 and 6 show close-up pictures at the foot of the bump and at the shock foot position, respectively. The grid is of course 3-D but is homogeneous in the z direction. Note that the x and y scales are approximately the same in Figs. 5 and 6.

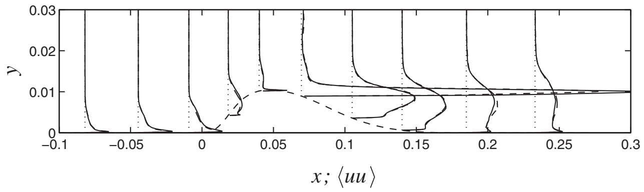

Fig. 8 Resolved $\langle uu \rangle$ Reynolds stresses: grid 1 (solid line); grid 2 (dashed line).

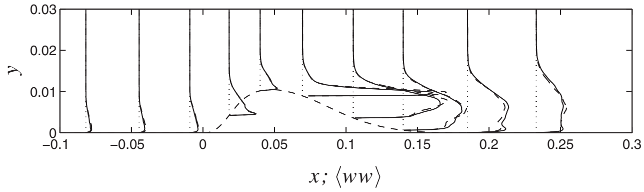

Fig. 9 Resolved $\langle ww \rangle$ Reynolds stresses: grid 1 (solid line); grid 2 (dashed line).

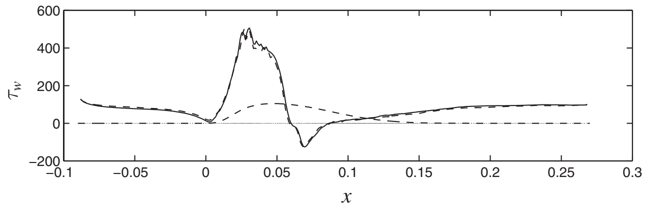

Fig. 10 Wall shear stress: grid 1 (solid line); grid 2 (dashed line).

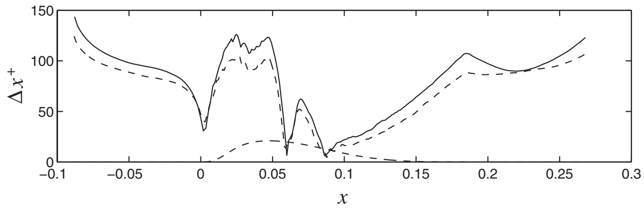

Fig. 11 Streamwise resolutions: grid 1 (solid line); grid 2 (dashed line).

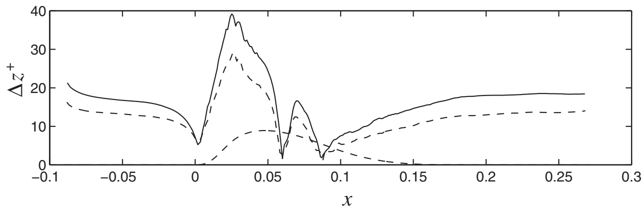

Fig. 12 Spanwise resolutions: grid 1 (solid line); grid 2 (dashed line).

To give an overview of the appearance of the flow, an average Mach contour plot is shown in Fig. 7. The Mach number before the shock is 1.27. The results from grid 1 and grid 2 were compared. No differences could be seen in first-order statistics, and most second-order statistics showed excellent agreement, as can be seen in Fig. 8. Only in the $\langle ww \rangle$ Reynolds stresses can slight differences between the two computations be seen (see Fig. 9). Note that the streamwise scale is different in Figs. 8 and 9 and that the bump has been rescaled to have the same *y* scale as the Reynolds stresses.

Another example of the near grid independence can be seen in Fig. 10 , which shows the average wall shear stress. The negative wall shear stress on the bump indicates strong shock-induced separation, and this is confirmed by the large amplification of the Reynolds stresses seen in Figs. 8 and 9. The grid resolution in terms of inner variables was calculated from the wall shear stress, and Δx^+ and Δz^+ are shown in Figs. 11 and 12. They more or less only confirm what has already been said about the resolution.

Grid 2 has slightly more cells in the streamwise direction than grid 1. As can be seen in Fig. 11, they were used to gain a generally better resolution, not only where Δx^+ were large but also in the vicinity of the shock. The reason for the refinement in the shock region is that almost no shock movement could be detected in the calculation on grid 1, whereas the shock was clearly moving in the experiments [18]. In this work, shock movement was measured by FFT of the shock position outside the viscous region. Shock movement in experiments may very well be caused by disturbances in the wind tunnel or unwanted 3-D effects. However, shock movement is often detected in computations of nominally 2-D flows, especially in supersonic flows, so the grid was refined in the streamwise direction to make sure that the lack of shock movement was not caused by low resolution. Despite the refinement, no shock movement could be detected. This is in disagreement with most experiments on transonic flows but is in agreement with the results of Sandham et al. [6].

As mentioned in Sec. IV.B, it is important that the computational results are not too dependent on the SGS model. For example, far from walls, the turbulent viscosity may at most be of the same order of magnitude as the kinematic viscosity. This can be seen by recalling the total diffusive term in the (incompressible) Navier–Stokes equation: $\partial/\partial x_j(\nu + \nu_t)(\partial \bar{u}_i/\partial x_j)$. In regions far from walls, the molecular diffusion influences only the high frequency part of the turbulent spectra. If ν_t/ν is much larger than 1, the whole turbulent spectra would be directly affected by the turbulence model, which is in contradiction with the fundamental large eddy assumption. However, a low value of ν_t/ν is not sufficient to be able to state that the subgrid model is good enough. Figure 10 shows that there is a plateau in τ_w before it reaches its minimum value. Compared with other experiments, a more typical configuration is a local minimum before the global minimum indicating preseparation before the large strongly separated region. Garnier et al. [7] made LES calculations of supersonic SWTBLI using higher Reynolds number and a more advanced subgrid model. Their results showed that, when the SGS model was turned off, the preseparation otherwise present disappeared. One possibility is, of course, that the low Reynolds number used in the calculations in the present case has increased the interaction length, hindering preseparation, but it cannot be excluded that a better subgrid model should be used. That investigation is discussed in Sec. VII.

On the basis of the small deviations in the Reynolds stresses and other statistical quantities, the good values of Δx^+, Δy^+, and Δz^+ and the low ν_t/ν, the only possible conclusion was that at least grid 2 had enough resolution for LES of this flow with a possible need for a better subgrid model.

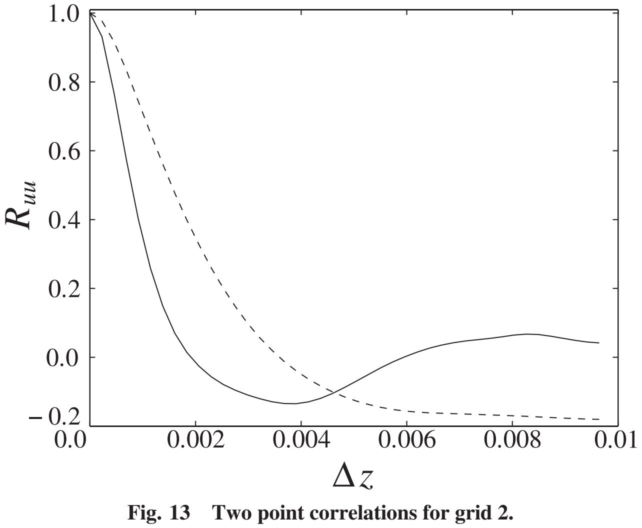

Fig. 13 Two point correlations for grid 2.

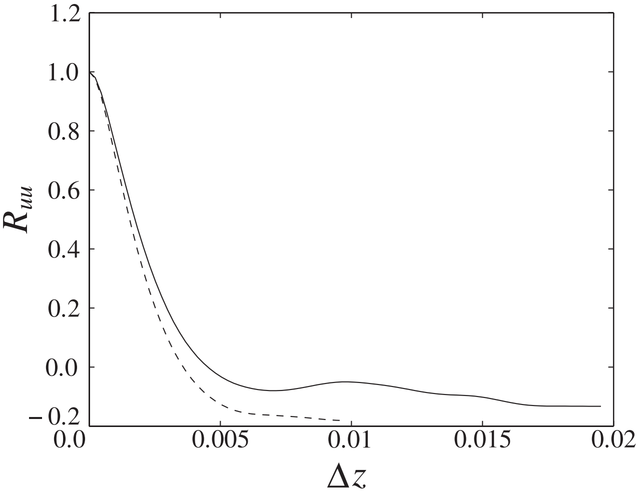

Fig. 14 Two point correlation at $x = 0.1155$, $y = 0.0076$: grid 3 (solid line); grid 2 (dashed line).

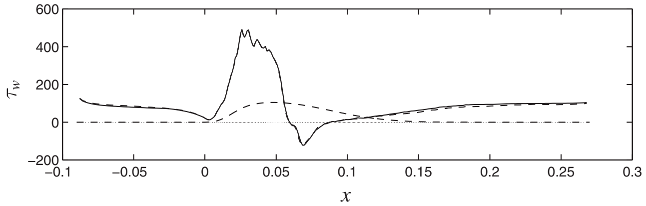

Fig. 15 Wall shear stresses: grid 3 (solid line); grid 2 (dashed line).

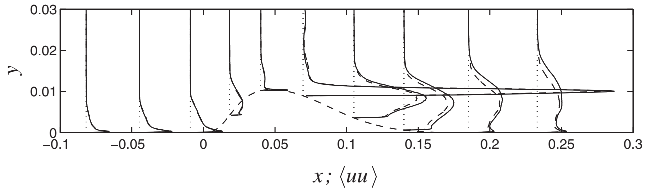

Fig. 16 Resolved $\langle uu \rangle$ Reynolds stresses: grid 3 (solid line); grid 2 (dashed line).

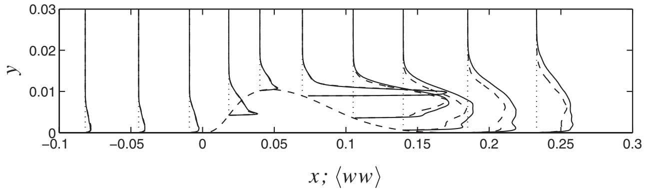

Fig. 17 Resolved $\langle ww \rangle$ Reynolds stresses: grid 3 (solid line); grid 2 (dashed line).

The important issue of domain width was investigated with two point correlations in the spanwise direction. For a domain to be wide enough, the two point correlations must vanish at a separation of half the domain width. Two point correlations are often normalized by their autocorrelations, and care must be taken so that the autocorrelations are not small compared with the maximum normal Reynolds stresses. Two point correlations were therefore calculated for several wall-normal distances, and only correlations strong enough were used in the analysis. Plotting two point correlations for several streamwise positions showed that the domain was wide enough to contain the largest spanwise structures of the boundary layer before the shock, but the larger structures a bit downstream of the shock were exactly half the domain width, which shows that the width was not sufficient. Figure 13 shows two typical correlation curves: one on the flat plate before the bump at $x = -0.0155$, $y = 0.00125$ (the solid line) and one behind the shock at $x = 0.1155$, $y = 0.0076$ (the dashed line). As can be seen, the two point correlation downstream of the shock takes large negative values for large Δz.

To meet the requirements of larger domain width, grid 3 was created. It had the same resolution as grid 2 but with twice the domain width, i.e., approximately 0.04 m instead of 0.02 m. In Fig. 14, one of the two point correlations from Fig. 13, the dashed line, is compared with the corresponding two point correlation computed from the results for grid 3. Apart from the somewhat strange behavior for large Δz, which will be treated in the next section, the correlation for grid 3 is satisfactory. Although only one example is shown in Fig. 14, it displays the general trend for the spanwise two point correlations. For first-order statistics, both primary data, such as velocity and wall pressure, and gradients did not change notably by the widening of the domain. An example of this can be seen in Fig. 15, where the wall shear stresses are compared. The Reynolds stresses on the other hand showed deviations that at most were somewhat less than 50%. The $\langle uu \rangle$ and $\langle ww \rangle$ Reynolds stresses are shown in Figs. 16 and 17, respectively.

50% deviation may sound like a rather large deviation, but it is partly an artifact of normalization. For example, $\max(\Delta\langle uu \rangle)/\max(\langle uu \rangle)$ is not more than 14%. However, also taking into account the two point correlations and the very good agreement in first-order statistics, the differences are not large enough to justify calculations on a grid even wider than grid 3.

VII. Improvement of the Calculations

All results presented thus far were achieved using a Smagorinsky model with constant filter width. As an improvement, but also as a check of the dependence on the subgrid model, the modeling of the total viscosity was improved. Not only was the Smagorinsky model replaced with the WALE model, but the perfect gas assumption was improved by prescribing that the viscosity would follow Sutherland's law [13].

To motivate the final change made, some analysis of the spanwise two point correlations is necessary. A very large amount of data is required to make those correlations converge, especially for large separations, and as can be seen in for example Fig. 14, the correlation for grid 3 exhibits oscillations that may well be caused by too few data samples. Figure 18 depicts the $\langle uu \rangle$ and the $\langle ww \rangle$ two point correlations at $x = -0.0145$ m, $y = 0.00125$ m. They fall off as expected for small Δz, but the relatively high correlations at $\Delta z \approx 0.0012$ m are not expected. It turns out that they originate from the inlet boundary conditions. Figure 19 shows the same correlations at the inlet ($x = -0.0891$ m, $y = 0.273$ mm), and both have sharp

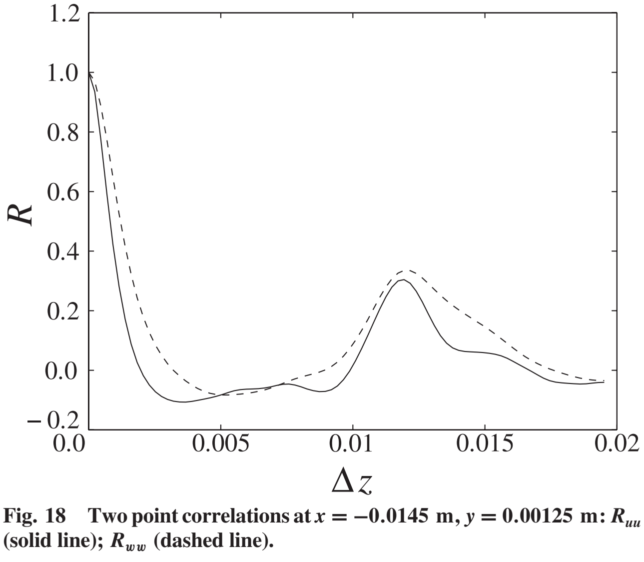

Fig. 18 Two point correlations at $x = -0.0145$ m, $y = 0.00125$ m: R_{uu} (solid line); R_{ww} (dashed line).

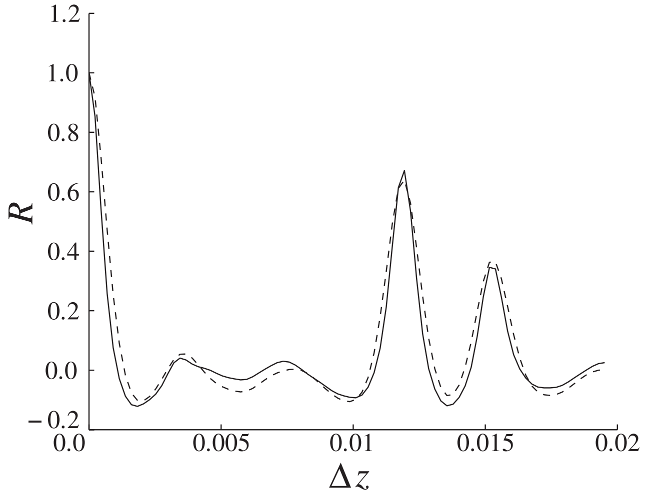

Fig. 19 Two point correlations at $x = -0.0891$ m, $y = 0.273$ mm: R_{uu} (solid line); R_{ww} (dashed line).

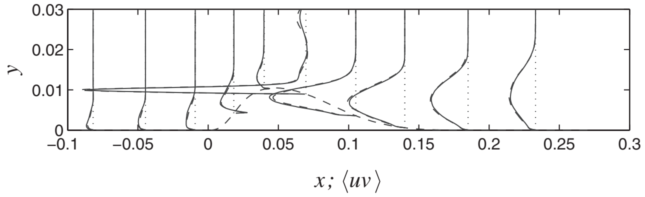

Fig. 20 Comparison of the resolved $\langle uv \rangle$ Reynolds stresses: WALE model (solid line); Smagorinsky model (dashed line).

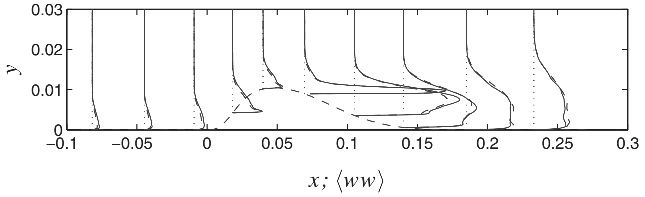

Fig. 21 Comparison of the resolved $\langle ww \rangle$ Reynolds stresses: WALE model (solid line); Smagorinsky model (dashed line).

Table 2 Mean separation and reattachment points for different subgrid models

Subgrid model	Separation point	Reattachment
WALE	$x = 0.059$ m	$x = 0.090$ m
Smagorinsky	$x = 0.059$ m	$x = 0.088$ m
No subgrid model	$x = 0.060$ m	$x = 0.087$ m

peaks at $\Delta z = 0.0119$ m and $\Delta z = 0.0153$ m as well as some smaller oscillatory peaks. As mentioned in Sec. IV.C, fluctuations from DNS data were added to a measured velocity profile, but the DNS data covered a width of only 1.2 cm. To cover all of the computational domain, the turbulent data were repeated until the whole domain was covered. This procedure is the cause of the peaks at $\Delta z = 1.2$ cm. The other peaks are a result of the same procedure, but they turn up at other Δz because the domain is covered by 3.28 repetitions of the DNS data, not an integer number.

It was clear from the beginning that the two point correlations would look like this directly after the inlet, but it was highly unexpected that the peaks would persist in the flow for such a long time. Even after the acceleration up the bump, the $\langle ww \rangle$ correlation shows a peak at $\Delta z \approx 1.3$ cm. There are no turbulent structures, at least not before the bump, that cause the high correlations for large Δz, rather the peaks are pure artifacts of the inlet boundary condition. And, because no unphysical structures are introduced, the computations are valid. However since this "pollution" in the spanwise two point correlations hinders drawing conclusions on the size of the turbulent scales, a new channel DNS was made with a width such that, when rescaled, it was equal to the width of grid 3.

The value of ν_t/ν is for the calculation using the WALE model in the order of unity with instantaneous values as large as 10. That is a considerable increment compared with the calculations using the Smagorinsky model. Despite this increase there are no large differences between the calculations. Figures 20 and 21 show the $\langle uv \rangle$ and $\langle ww \rangle$ Reynolds stresses. The $\langle uv \rangle$ stresses are representative for the magnitude of deviations between the calculations on grid 3 using the Smagorinsky and the WALE models. The $\langle ww \rangle$ exhibit the largest deviations, but they are still very small. It is also worth noting that the shock does not show any large scale movement despite the more advanced subgrid model.

Both the Smagorinsky model and the WALE model are algebraic turbulent eddy viscosity models, and the good agreement between the models could be a result of their close relationship. Hence, before making any assessment of the subgrid model dependence, results from a simulation without any subgrid model at all are discussed. Once again, first-order statistics do not change, i.e., the general picture of the flow remains unchanged. The differences in Reynolds stresses between the simulation using the WALE model and this latest simulation without a subgrid model are of the same order as those shown in Figs. 20 and 21. The largest difference is found in the mean separation length calculated from the points where the wall shear stress changes sign. The results are presented in Table 2. Notice though that these differences are quite small, at most 13%.

The good agreement between the results of the calculations using different subgrid models and no subgrid model shows that the results are virtually independent of the subgrid model used. This is consistent with the previous statement that the LES is very well resolved. Since the numerical scheme is low dissipative, the only question mark left is the shock-capturing term described by Eq. (16). Such a term always introduces extra dissipation which can be as large as the subgrid dissipation. This shock-capturing term remains, however, negligible everywhere compared with the diffusive fluxes even if the subgrid model is removed, except of course in the shock.

Finally, before proceeding with the analysis of the flow, we notice that there is no need for a reinvestigation of the grid resolution or the domain width because the small deviations in the results would not lead to any new conclusions and the spanwise two point correlations show no sign of peaks as those depicted in for example Fig. 19, which confirms that the peaks were artifacts of the way in which the inlet boundary conditions were created.

From here on, only data from the simulation on grid 3 using the WALE model will be discussed.

VIII. Comparison with Experiments

Comparison with experiments is not easy for several reasons. The only quantity that was directly measured was the wall pressure [18]. The shock frequency was calculated from a series of Schlieren visualization and Mach numbers approximated by using pressure and temperature in a stagnation chamber. Consequently, there are few possibilities to validate how well the experiments are predicted by the calculations, but those comparisons that can be made will be presented. The experimental case that comes closest to the LES is chosen.

A qualitative comparison is shown in Figs. 22 and 23. As can be seen, the shock is located at the same x position and covers the same fraction of the channel height. The shock given by the LES calculation is, however, more normal than in the experiments. The difference can be explained by the mass flow that is locally different in the two cases. In the experiments, oil visualization showed large separation zones at the side walls. Oil visualization from the same experimental case as above is shown in Fig. 24. As can be seen, these separation zones cover more than 50% of the cannel width, and the mass flow is hence locally much larger in the experiments.

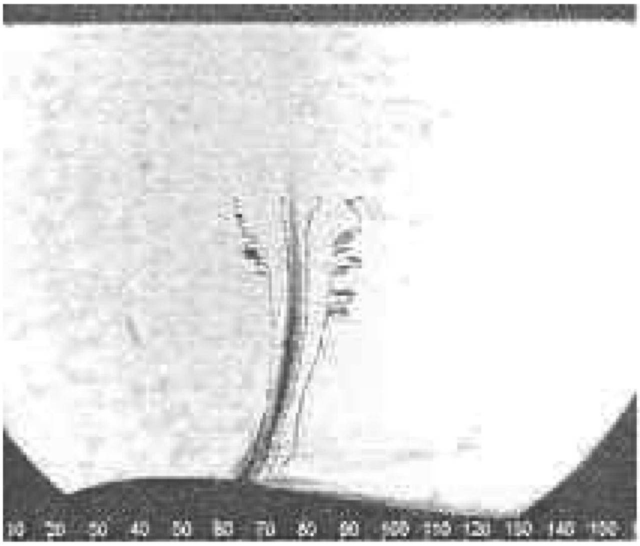

Fig. 22 Schlieren picture from experiments [18] with outlet pressure equal to 106 kPa. Same scale as in Fig. 23. The solid lines indicate the extreme positions of the shock.

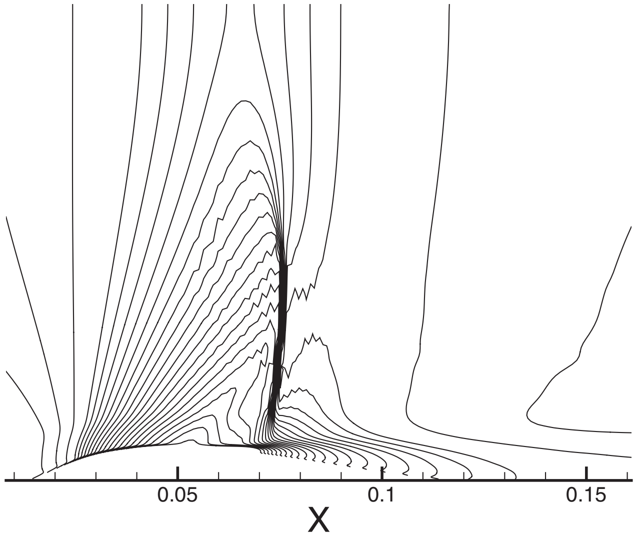

Fig. 23 Density contours from calculation on grid 3 using the WALE model.

In Fig. 25, the wall pressure coefficient for the LES is compared with that of the experiments. The pressure coefficients are calculated by

$$c_p = \frac{p - p_{x=-0.09\ \mathrm{m}}}{p_{\mathrm{dyn},x=-0.09\ \mathrm{m}}} \tag{20}$$

The sidewall separation starts about half a centimeter before the shock foot location, and the blockage gives extra acceleration that in turn gives a stronger shock than would be the case without the sidewall separation. Both the extra strength of the experimental shock and the sidewall separation give extra pressure loss, which is the explanation of why the pressure coefficient in the LES settles at a higher level than in the experiments.

Compared with the experiments, the most noticeable difference is the lack of large scale shock movement. It could be seen that there really is no shock movement from both FFT of the shock position and from animations of the flowfield. When an FFT is made of the shock position and the power spectrum is plotted as a function of the frequency, only a sharp peak at $f = 0$ Hz with $P_h(f = 0) = 0.07$ (the mean shock position) is visible, the power on every other frequency being at least 100 times smaller.

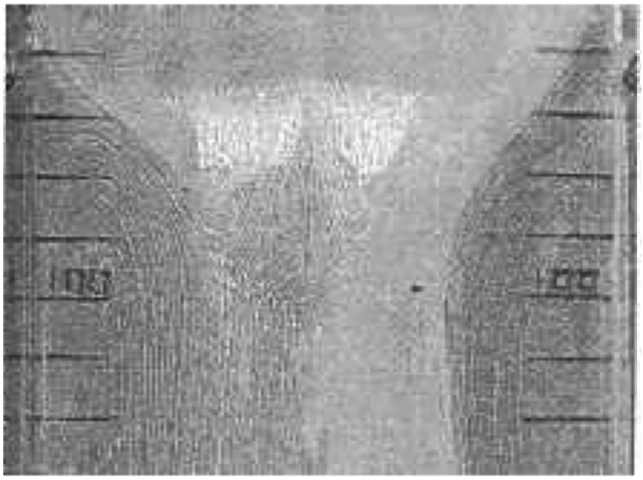

Fig. 24 Oil visualization from experiments [18]. The distance between the lines at the side is 1 cm.

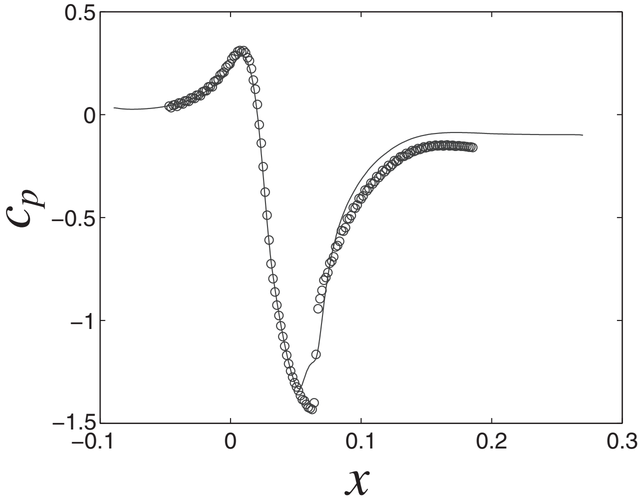

Fig. 25 Pressure coefficient: LES (solid line) and experiments (○).

It is not clear exactly what frequency region in which shock oscillations can be expected. Measurements made by Bron [18] show that the shock frequency is very low, mostly in the region of 0–100 Hz with a single peak at 350 Hz. It is possible that the simulation length of 5 ms is too short to resolve shock oscillations. However in Bron's measurements, the shock moved over a $\Delta x \approx 1$ cm (the solid lines in Fig. 22), and the shock is absolutely stable during the 5 ms simulated here. If the largest amplitude was connected to a frequency of, for example, 100 Hz, at least half a revolution would have been visible, resulting in the shock traveling a total of 1 cm. That leaves only three possible explanations. One is that the large scale shock movements have frequencies in the order of 10 Hz, but that is much slower than any other characteristic time scale in the flow, especially those considered candidates for shock movement, for example, the separation bubble and the incoming boundary layer. This leads to the second possible explanation. The large scale shock movements in the experiments may be caused by disturbances in the wind tunnel facility. The third and last possible explanation is that the altered Reynolds number has altered the flowfield and thereby ruled out shock movement.

It is a bit dangerous to use such a simple outlet boundary condition as constant static pressure. Most computations made today use buffer zones to prevent reflections at the outlet, reflections that result in artificial sound waves traveling upstream. If such artificial reflections reach the shock, they might interact with it to cause unphysical shock movement or, as can be suspected in this case, to prevent shock movement. However, the only way these waves can prevent shock movement is if some of their frequencies are resonance frequencies of the shock *and* if they have exactly the opposite phase of whatever physical phenomena that would have produced shock movement if the artificial sound waves were not present. The risk that this is the situation is negligible but can be ruled out completely only if a buffer region is introduced.

We conclude that the simulation on grid 3 comes as close to the experiments as possible.

IX. Flow Studies

The previous sections have shown that the LES is a highly realistic simulation of the transonic case and that it is as close as possible to the experimental case measured by Bron. There are, however, differences, most noticeably the lack of large scale shock movement in the simulation. The current simulation cannot be used to explain this difference, but the results can be used to rule out possible explanations for shock movement.

A. Separation Characteristic

Shock oscillation seems at least partly to be connected to a possible separation of the boundary layer with only small oscillations if there is no, or weak, separation [18]. The concept of incipient separation and its detection is thoroughly treated in [2]. There is incipient separation when τ_w is positive everywhere except for one point at which it equals zero. As can be seen in Fig. 15, the flowfield considered here is well beyond incipient separation. For the flow to be effectively separated, there must be a sizable region in which the probability of backflow is greater than 0.5. In Figs. 26 and 27, the PDF of the skin-friction coefficient is given as a function of the streamwise position x. The distribution includes instantaneous data from all spanwise positions. As can be seen, the presence of the shock is first felt by the fluid at $x \approx 0.045$ m, resulting in a decrease in C_f, but the variance of the distribution of C_f is not changed until the fluid reaches $x \approx 0.06$ m, where the variance increases drastically, indicating effective separation with high intermittency. The probability of backflow can be found by integrating the PDF for all negative C_f; the result is shown in Fig. 28. Clearly, there is a separated region, $P(C_f < 0) > 0.5$, of 3 cm ranging from $x \approx 0.06$ m to $x \approx 0.09$ m.

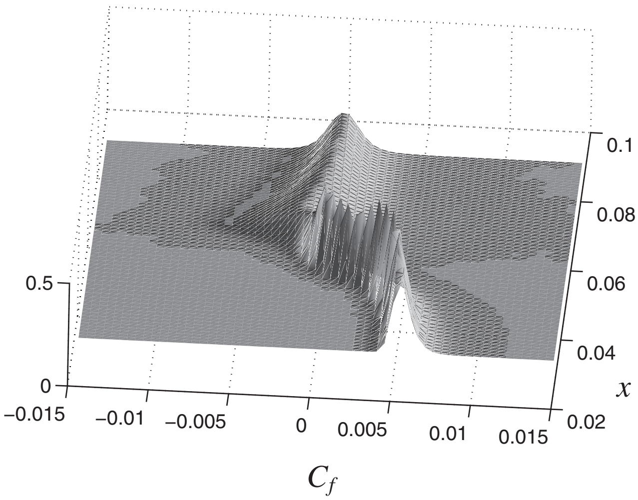

Fig. 26 3-D visualization of the PDF of C_f.

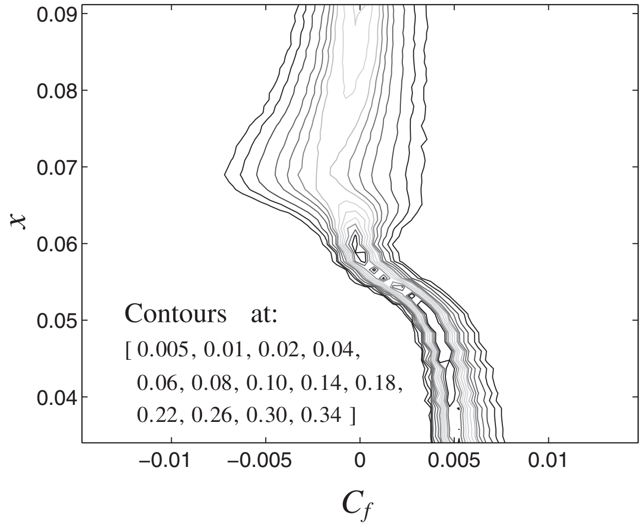

Fig. 27 Contour lines of the PDF of C_f.

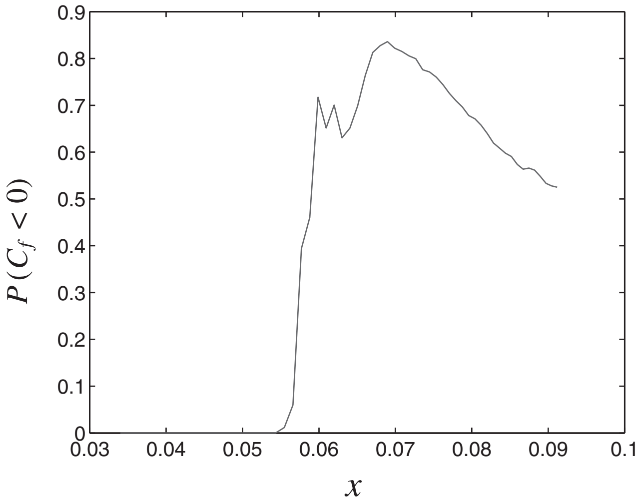

Fig. 28 Probability for $C_f < 0$ as a function of streamwise position.

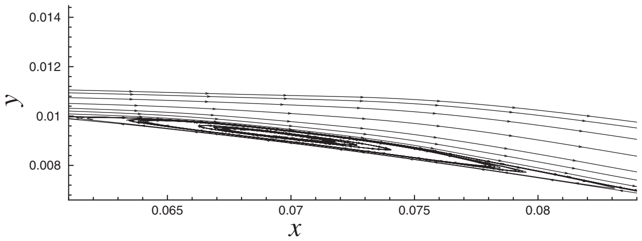

Fig. 29 Streamlines calculated from the average solution.

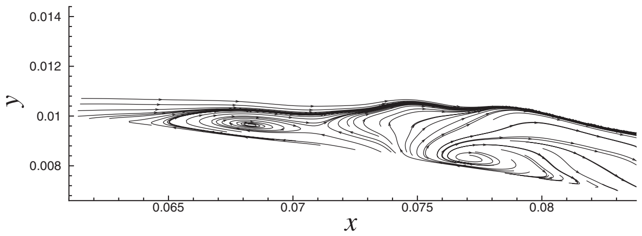

Fig. 30 Streamlines calculated from an instantaneous solution.

Although 3 cm is in this case a rather large length scale, it is not clear that the separated region can be considered sizable. Figure 29 depicts streamlines calculated from the average solution; as can be seen, the separation bubble is merely 1 mm high. On the other hand, visualizations of instantaneous solutions of the flowfield reveal a different picture. An example is given in Fig. 30. It is obvious that the mean flowfield in the separated region bears little resemblance to the real flow structures, which are not stationary anywhere and are several millimeters high. Thus the seemingly low height of the separation region is a result of there being several recirculation bubbles that are not stationary. In other words, if the flow is studied using first-order statistics, the separation is concealed by the large Reynolds stresses.

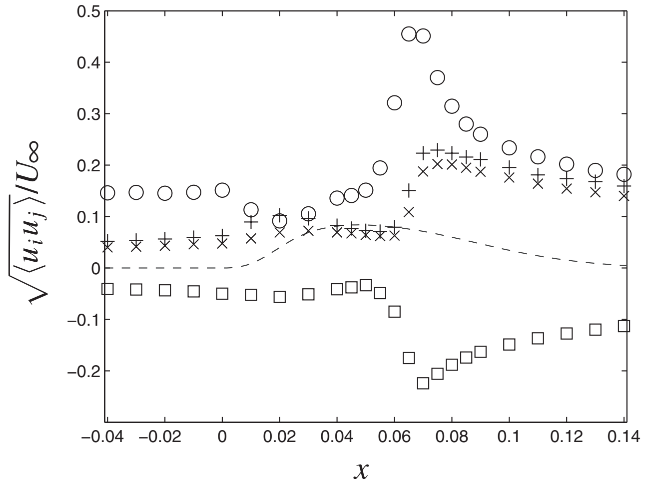

Fig. 31 Normalized maximum values of the Reynolds stresses: ○ = $\sqrt{\langle uu \rangle}/U_\infty$; × = $\sqrt{\langle vv \rangle}/U_\infty$; + = $\sqrt{\langle ww \rangle}/U_\infty$; □ = $\sqrt{|\langle uv \rangle|}/U_\infty$ (sign restored). The dashed line is the wall profile.

Further evidence for strong separation is given in Fig. 31, which shows the extreme values of the Reynolds stresses. It can be seen that $\sqrt{\langle uu \rangle}/U_\infty$ rises by more than 300% as the fluid passes through the interaction region. According to data in [2], such high rises in $\sqrt{\langle uu \rangle}/U_\infty$ indicate strong separation. Also visible is the high degree of anisotropy after the SWTBLI, which is expected because the shock is a mostly nonisotropic phenomenon [23]. As seen in Fig. 32, the distances to the wall for the maxima of the Reynolds stresses move towards the wall as the boundary layer is retarded by the adverse pressure gradient preceding the shock. What looks like asterisks in Fig. 32 are the plus and the cross symbols that happen to fall at the same wall distances. As the fluid passes through the separation region, turbulence is thrown out from the wall where it creates a strong turbulent region, possibly a vortex sheet. This region is clearly visible in for example Fig. 21.

Most statistical limits for separation do not take into account the curvature of the wall, and the concept of effective separation is a bit vague. The important point here is that the flow features strong unsteady structures under the shock, structures that may be a source of shock movement. The PDF of C_f and the comparison between the average and instantaneous streamlines show that there is separation and that the flowfield is highly unstable. The structures are, furthermore, strong in the sense that the Reynolds stresses are amplified by several hundred percent.

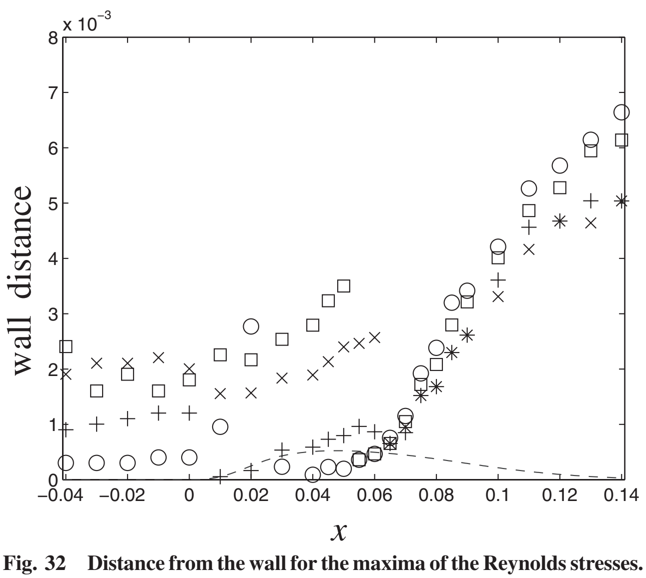

Fig. 32 Distance from the wall for the maxima of the Reynolds stresses. ○ = $\sqrt{\langle uu \rangle}/U_\infty$; × = $\sqrt{\langle vv \rangle}/U_\infty$; + = $\sqrt{\langle ww \rangle}/U_\infty$; □ = $\sqrt{|\langle uv \rangle|}/U_\infty$. The dashed line is the wall profile.

B. Reynolds Number Effects

The boundary layer was designed to have correct turbulence intensity at the inlet and to match the thickness of the experimental boundary layer at the bump foot. However, as the flow is accelerated up the bump, it is influenced by a favorable pressure gradient that starts a relaminarization process whose rate is proportional to the viscosity. Jones and Launder [24] describe the acceleration parameter

$$K = \frac{\nu}{U_\infty^2} \frac{\partial U_\infty}{\partial s} \tag{21}$$

where $\partial/\partial s$ represents derivative in the streamwise direction and U_∞ represents the freestream velocity parallel to the wall. For relaminarization to occur, K should be larger than 3×10^{-6} over a long enough streamwise distance. For this computation K reaches above that limit, but as can be seen in Fig. 31, the boundary layer remains turbulent for all x.

It is stated in [2] that the strength of the separation is dependent on the incompressible form factor defined by

$$H = \frac{\delta^*}{\theta} = \frac{\int_0^{\delta_{99}} (1 - U/U_\infty)\,\mathrm{d}n}{\int_0^{\delta_{99}} (U/U_\infty)(1 - U/U_\infty)\,\mathrm{d}n} \tag{22}$$

but independent of the Reynolds number. In Eq. (22) dn represents integration in the wall-normal direction and U once again represents the velocity parallel to the wall. The flow should feature strong separation with recirculation only if the shock is strong enough to force H to become larger than 2.6, the exact number depending on the curvature of the wall. This number is close to 2.7, which was obtained as a separation criterion by Castillo et al. [25] in their similarity analysis of incompressible equilibrium boundary layers. In the current calculations, however, the Reynolds number has a direct effect because a lower Reynolds number gives a lower form factor as the flow is accelerated. The form factor for the current case is plotted as a function of x in Fig. 33. It is never in any position near 2.6, yet strong separation does occur and the curvature of the wall is not strong enough to explain this large deviation in maximum form factor from the conventional value. Obviously, the relation between the incompressible form factor and the separation characteristic must be further investigated.

C. Space and Time Scales

Having proved that the flow does indeed feature SWTBLI with strong separation, attention will now be given to the space and time scales appearing in the SWTBLI. There are several candidates in flow phenomena that trigger large scale shock movement. Those present in this computation can at least be excluded as triggering

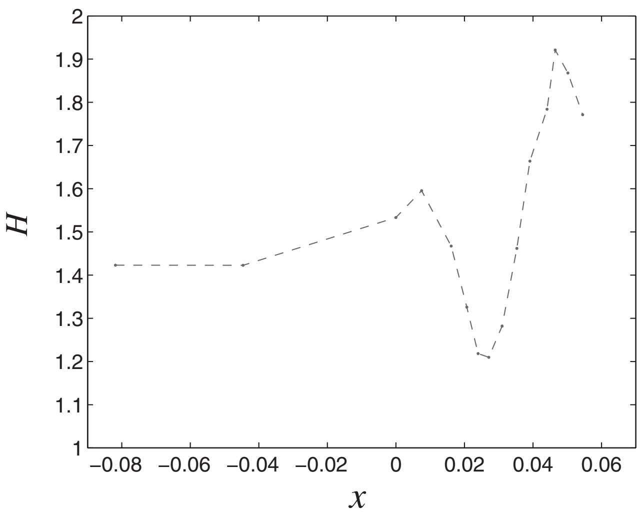

Fig. 33 Form factor of the boundary layer as function of streamwise position x.

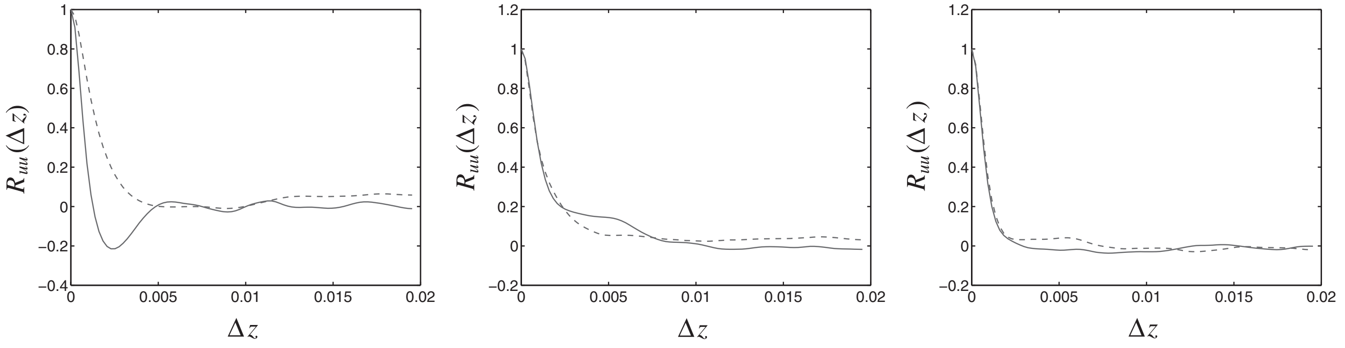

a) ***x*** **= 0.005 m** **b)** ***x*** **= 0.06 m** **c)** ***x*** **= 0.07 m**

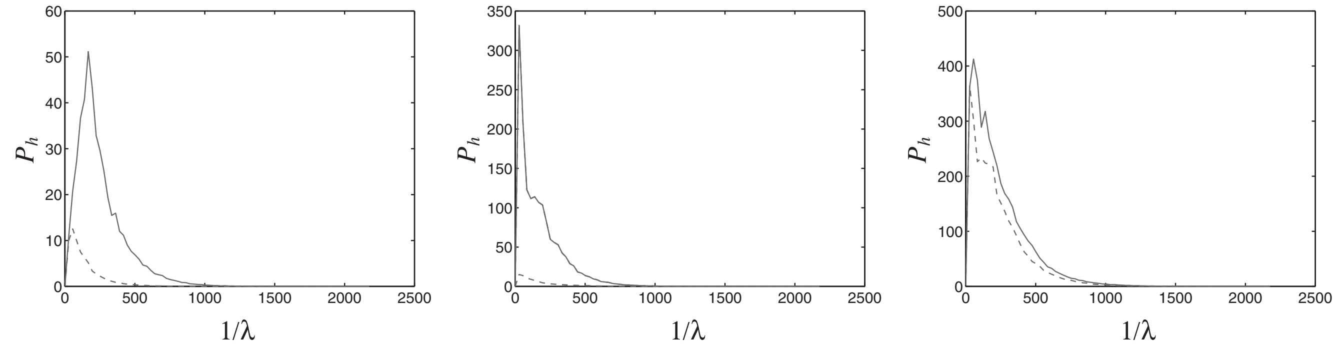

d) ***x*** **= 0.005 m** **e)** ***x*** **= 0.06 m** **f)** ***x*** **= 0.07 m**

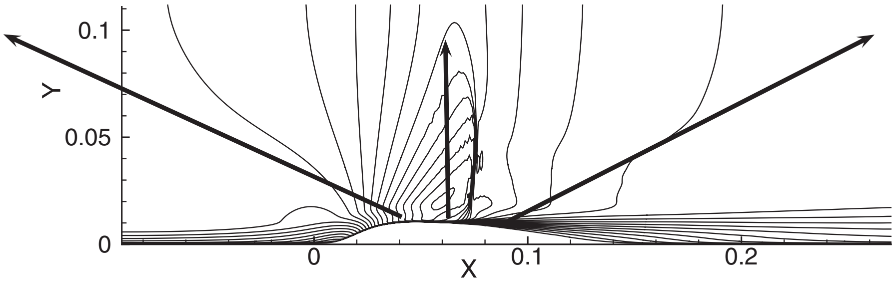

Fig. 34 Spatial correlations in the spanwise direction and their power spectra taken at approximately 0.5 mm (solid lines) and approximately 1 mm (dashed line) from the wall.

events, although they can still be events determining the frequency of the shock movement if something else, not present in this computation, triggers it.

The connection between flow structures and unsteady shock movement has been chiefly investigated for supersonic flow in a compression ramp. Thomas et al. [26] related the shock movement to the frequency of the separated region. There are significant differences between the current case and the supersonic one. In the supersonic case, the separation bubble is "trapped" between the shock and the compression ramp, whereas the current flow features not one but several separation bubbles. Thus, no single turnover time can be computed for the current case, although the analogy can still be useful. On the other hand, several investigations of supersonic compression ramp flow have pointed out the bursting frequency of the incoming boundary layer to be the frequency of the shock movement. See, for example, [27,28].

There is no unambiguous method for calculating the size of the largest turbulent structures. If, for example, the *uu* time correlation is considered, structures like the ones shown in Fig. 30 can be argued, using the concept of frozen turbulence, to make negative contributions to the time correlations. That makes, for example, the ordinary interpretation of the integral time scale questionable. Correlations, both in time and space, and their power spectra can on the other hand be computed in one way only and will be used instead. Three streamwise positions will be investigated, $x = 0.05$ m, $x = 0.06$ m, and $x = 0.07$ m, which roughly correspond to the beginning of the interaction zone, the separation point, and the region where C_f is most likely to be negative, respectively, (see Fig. 27).

Figure 34 shows some two point correlations and their power spectra for the three positions taken at two fixed distances from the wall. Because the flow in the region currently discussed is separated, viscous units make no sense. However, at $x = 0.05$, they correspond to distances of 20 and 100 viscous units from the wall. Figure 35 shows autocorrelations and corresponding power spectra taken at the same positions.

The first interesting characteristic can be found in Fig. 34a where the near-wall space correlation shows oscillating behavior. Figure 34d reveals that the wavelength is 6 mm, which corresponds to $\Delta z^+ \approx 300$. A possible explanation is the streamwise rolls, which are characteristic for turbulent boundary layers (see, for example, [29]). They cannot be detected further out in the boundary layer, however, and it can also be observed that much less energy is contained in turbulent structures there. This is consistent with the findings of Ichimiay et al. [30] that show that relaminarization begins from the outer part of the boundary layer.

The autocorrelations taken at $x = 0.05$ m also show oscillating behavior (Fig. 35a), and their power spectra, shown in Fig. 35d, reveal a distinct peak at about 5500 Hz. This frequency can be connected to the bursting events mentioned at the beginning of this section. To detect possible burst events in the incoming boundary

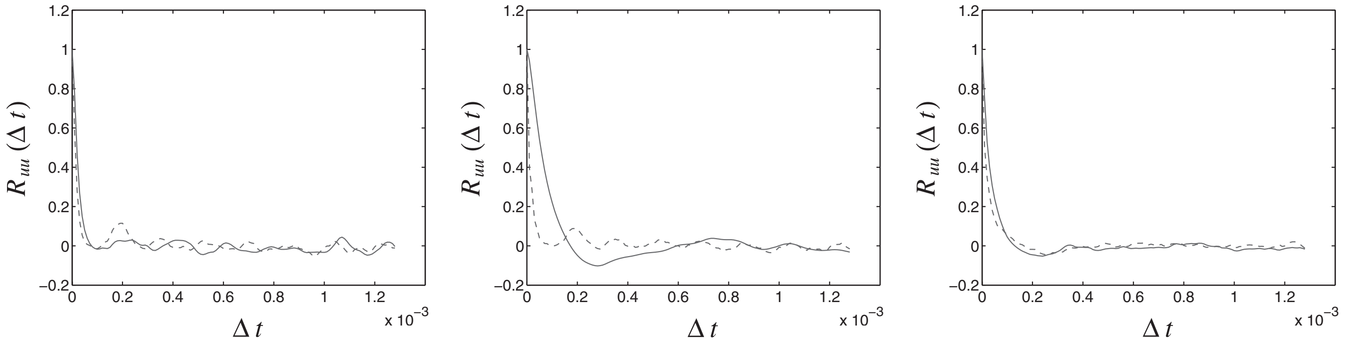

a) x **= 0.005 m** **b)** x **= 0.06 m** **c)** x **= 0.07 m**

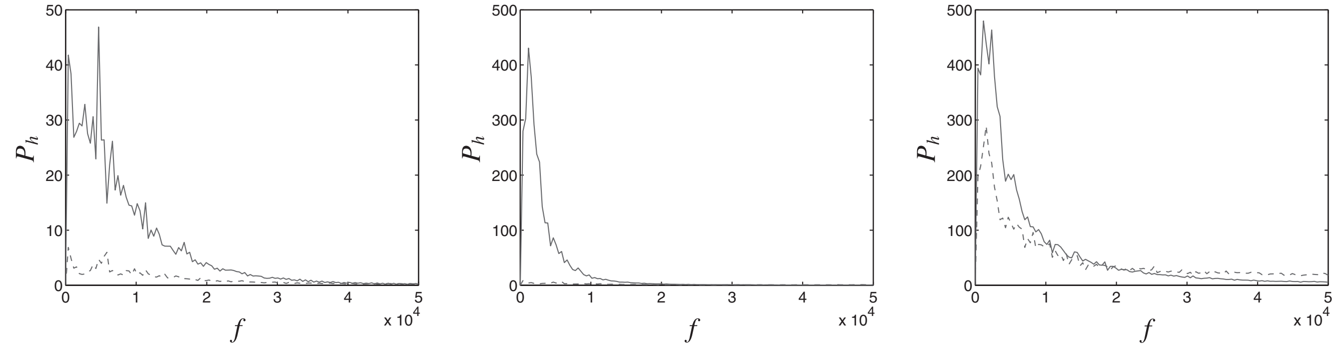

d) x **= 0.005 m** **e)** x **= 0.06 m** **f)** x **= 0.07 m**

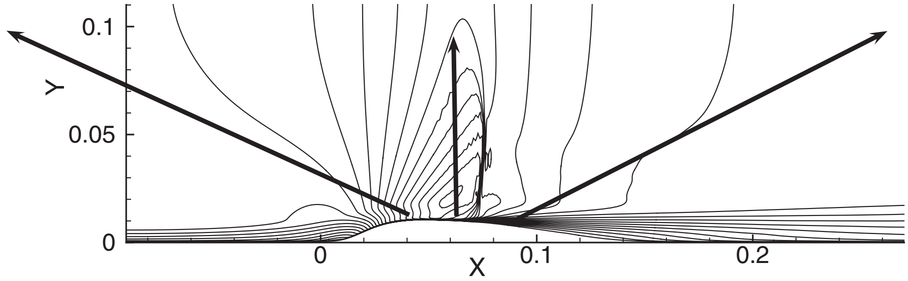

Fig. 35 Autocorrelations and their power spectra taken at approximately 0.5 mm (solid lines) and approximately 1 mm (dashed lines) from the wall.

layer of the current case, an indicator function was applied at a distance of $0.5\delta_{99}$ from the wall at $x = 0.05$ m. The indicator function, I_M, was defined by

$$I_M = \begin{cases} 1 & \text{if } M > \bar{M} + \sigma_M \\ -1 & \text{if } M < \bar{M} - \sigma_M \\ 0 & \text{otherwise} \end{cases} \tag{23}$$

where σ_m is 1 standard deviation of the Mach number distribution in the point where I_M is measured. This is the same indicator function that was applied by Wu and Martin [28]. They found that bursts and shock movement had a main frequency of $0.14U_\infty/\delta$, which in this case would be approximately $0.14 \times 330/0.008 = 5.8$ kHz. The result is displayed in Fig. 36 where a few important frequencies can be seen, and the highest peak is at 5500 kHz, which is the sought-after phenomenon. There are also other peaks that are almost as strong, and it is possible that each peak corresponds to a specific burstinglike event.

The incoming boundary layer is dominated by the streamwise rolls in the spanwise direction and the bursting process in time. As the flow reaches the point of separation, the streamwise rolls can still be detected close to the wall (Fig. 34b), but as can be seen in Fig. 34e, there is a shift toward larger structures. Observe that the lowest peak in Fig. 34e represents the periodicity of the domain and not necessarily a real structure. The bursting frequency of the incoming boundary layer can still be detected, at least a bit out from the wall (Fig. 35b), but a new time scale of frequency 1.2 kHz has been introduced close to the wall (Figs. 35b and 35e). This new time scale is not captured by the indicator function and is thus not a bursting process. Instead, it is possible that the larger spanwise structures and the longer time scale found at the separation point ($x = 0.06$ cm) are connected to the separated region. There, they are the dominating scales (see Figs. 34f and 35f). But it is equally possible that these structures are created by the separation itself and swept downstream.

To investigate this matter the time-space correlation,

$$R_{uu}(x, \Delta t) = \frac{\langle u'(x = 0.064, t)u'(x, t + \Delta t)\rangle}{\sqrt{\langle u'(x = 0.064, t)^2\rangle}\sqrt{\langle u'(x, t)^2\rangle}} \tag{24}$$

was calculated along a gridline approximately 0.5 mm from the surface. Averaging is made in time and spanwise directions, but because space-time correlations contain more data than correlations in only space or time, Eq. (24) is not as well converged as those shown in Figs. 34 and 35. Fourier transforms in time of the time-space correlations can be written as

$$\mathcal{F}(R_{uu})(x, f) = |\mathcal{F}(R_{uu})(x, f)|e^{-\iota\Theta(x,f)} \tag{25}$$

where $|\mathcal{F}(R_{uu})(x, f)|$ is the magnitude of the frequency content and $\Theta(x, f)$ is its phase. The magnitude is shown in Fig. 37 and the phase in Fig. 38. Note that the sharp edge in the phase plot is a phase shift of 2π and that the lowest peak in the magnitude plot is due much to the

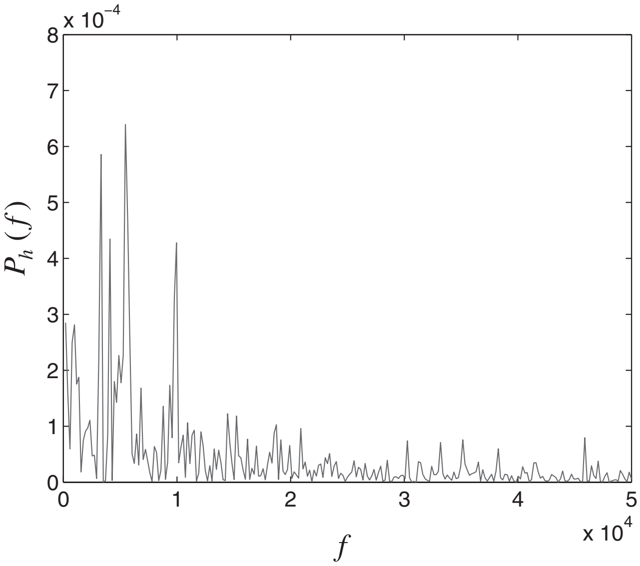

Fig. 36 Power spectrum of the indicator function I_M.

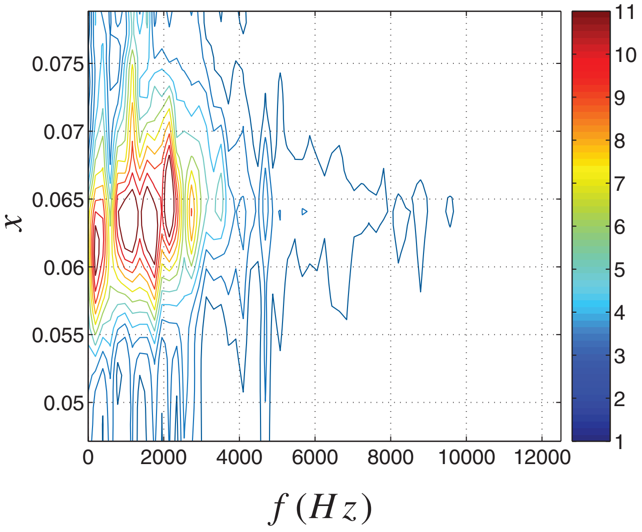

Fig. 37 Magnitude of space-time correlation Fourier transformed in time.

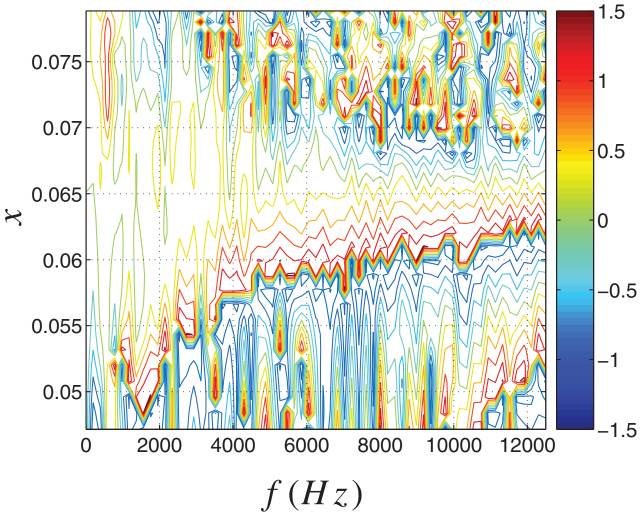

Fig. 38 Phase plot of space-time correlation Fourier transformed in time.

periodicity of time domain assumed when making the Fourier transform. The spectrum along the line $x = 0.064$ does, of course, reassemble Fig. 35e but with more energy in the frequency 2 kHz. As can be seen looking at the phase plot in Fig. 38, all frequencies larger than 1 kHz are traveling upstream from the separated region, whereas only the lowest frequencies are convected downstream. No frequency of interest seems to be created at the separation point, rather all frequencies seem to emanate from either upstream or downstream.

In conclusion, information both from the incoming boundary layer and from the separated region can be found at the separation point. Thus, although the flow case possesses qualities necessary for the separated region to induce low frequent shock movement, it does not.

X. Conclusions

The results of a LES of transonic flow with SWTBLI have been presented. The computation is highly accurate with good resolution, a wide enough domain, and little dependence on the subgrid model. Comparison with experiments showed that the case is as close to experiments as possible, and hence, the simulation will make an excellent contribution to the database at KTH.

The flow is strongly separated in terms of probability for backflow as well as in terms of increase in time scales and Reynolds stresses through the interaction region. Such a flow case is commonly associated with low frequency large scale shock movement, usually believed to be triggered by either bursting events in the incoming boundary layer or events taking place in the separated region. In this calculation, however, no such shock movement could be detected.

The high viscosity made the form factor of the incoming turbulent boundary layer very low, and it never reached the conventional 2.6 before separation. This suggests that the concept of strong separation and its coupling to large scale shock movement needs further investigation.

A bursting frequency of 5.5 kHz was found in the incoming boundary layer as were streamwise rolls. These phenomena could also be found at the separation point. In the separated region, longer time scales and larger spanwise scales dominated, and information on those were found to be brought upstream through the subsonic boundary layer. In conclusion, the flow structures that are the most probable to trigger shock movement are all present, and they all influence the flow at the shock foot position. Findings presented here do not exclude the possibility for these structures to determine the actual frequency of shock movement once the proper conditions for such movement are fulfilled.

Acknowledgments

This project is sponsored by the Swedish Energy Agency and is a cooperative work with the Royal Institute of Technology, which has provided us with expreimental data. Some of the computations have been performed using resources supplied by Swedish National Infrastructure for Computing (SNIC).

References

[1] Dolling, D. S., "Fifty Years of Shock-Wave/Boundary-Layer Interaction Research: What Next?," *AIAA Journal*, Vol. 39, No. 8, 2001, pp. 1517–1531.

[2] "Shock-Wave Boundary Layer Interactions," AGARD, AGARDograph No. 280, 1986.

[3] Beresh, S. J., Clemens, N. T., and Dolling, D. S., "Relationship Between Upstream Turbulent Boundary-Layer Velocity Fluctuations and Separation Shock Unsteadiness," *AIAA Journal*, Vol. 40, No. 12, 2002, pp. 2412–2422.

[4] Bur, R., Benay, R., Corbel, B., and Delery, J., "Physical Study of Shock-Wave/Boundary-Layer Interaction Control in Transonic Flow," AIAA Paper 2000-0933, 2000.

[5] Knight, D., Yan, H., Panaras, A. G., and Zheltovodov, A., "Advances in CFD Prediction of Shock Wave Turbulent Boundary Layer Interactions," *Progress in Aerospace Sciences*, Vol. 39, No. 4, 2003, pp. 122–184.

[6] Sandham, N. D., Yao, Y. F., and Lawal, A. A., “Large-Eddy Simulation of Transonic Turbulent Flow over a Bump,” *International Journal of Heat and Fluid Flow*, Vol. 24, No. 4, 2003, pp. 584–595.

[7] Garnier, E., Sagaut, P., and Deville, M., “Large Eddy Simulation of Shock/Boundary-Layer Interaction,” *AIAA Journal*, Vol. 40, No. 10, 2002, pp. 1935–1944.

[8] Eriksson, L.-E., “Development and Validation of Highly Modular Flow Solver Versions in g2dflow and g3dflow Series for Compressible Viscous Reacting Flow,” Volvo Aero Corporation, Internal Rept. 9970–1162, Sweden, 1995.

[9] Wollblad, C., “Large Eddy Simulation OF Transonic Flow with Shock Wave/Turbulent Boundary Layer Interaction,” Licentiate of Engineering thesis, Dept. Thermo and Fluid Mechanics, Chalmers University of Technology, Gothenburg, Sweden, 2004.

[10] Andersson, N., “A Study of Mach 0:75 Jets and Their Radiated Sound Using Large-Eddy Simulation,” Licentiate of Engineering thesis, Dept. Thermo and Fluid Mechanics, Chalmers University of Technology, Gothenburg, Sweden, 2003.

[11] Erlebacher, G., Hussaini, M. Y., Speziale, C. G., and Zang, T. A., “Toward the Large-Eddy Simulation of Compressible Turbulent Flows,” *Journal of Fluid Mechanics*, Vol. 238, 1992, pp. 155–185.

[12] Nicoud, F., and Ducros, F., “Subgrid-Scale Stress Modelling Based on the Square of the Velocity Gradient Tensor,” *Flow, Turbulence and Combustion*, Vol. 62, No. 3, 1999, pp. 183–200.

[13] Schlichting, H., *Boundary-Layer Theory*, 7th ed., McGraw–Hill, New York, 1979.

[14] Martensson, H., Eriksson, L.-E., and Albraten, P., “Numerical Simulations of Unsteady Wakeflow,” *Proceedings of the 10th International Symposium on Air Breathing Engines*, International Society for Air Breathing Engines Paper 9370-309, 2001.

[15] Jameson, A., Schmidt, W., and Turkel, E., “Numerical Solutions of the Euler Equations by Finite Volume Methods Using Runge-Kutta Time-Stepping Schemes,” AIAA Paper 81-1259, 1981.

[16] Laney, C. B., *Computational Gasdynamics*, Cambridge Univ. Press, New York, 1998.

[17] Wollblad, C., Davidson, L., and Eriksson, L.-E., “Semi-implicit Preconditioning for Wall-bounded Flow,” AIAA Paper 2004-2135, 2004.

[18] Bron, O., “Numerical and Experimental Study of the Shock-Boundary Layer Interaction in Transonic Unsteady Flow,” Ph.D. thesis, Royal Institute of Technology, Sweden, 2003.

[19] Sigfrids, T., “Hot Wire and PIV Studies of Transonic Turbulent Wall-Bounded Flows,” Licentiate of Engineering thesis, Dept. of Mechanics, Royal Institute of Technology, Sweden, 2003.

[20] Welty, J. R., Wicks, C. E., and Wilson, R. E., *Fundamentals of Momentum, Heat, and Mass Transfer*, Wiley, New York, 1984.

[21] Johansson, G., and Castillo, L., “LDA Measurements in Turbulent Boundary Layers with Zero Pressure Gradient,” *Proceedings of Turbulence and Shear Flow Phenomena, 2nd International Symposium*, edited by E. Lindborg, A. Johansson, J. Eaton, J. Humphrey, N. Kasagi, M. Leschziner, and M. Sommerfeld, The Royal Institute of Technology, Stockholm, Sweden, 2001, pp. 15–20.

[22] Piomelli, U., and Chasnov, J., “Large-Eddy Simulations: Theory and Applications,” *Transition and Turbulence Modelling*, edited by D. Henningson, M. Hallbaeck, H. Alfredsson, and A. Johansson, Kluwer Academic, Norwell, MA, 1996, pp. 269–336.

[23] Rotta, J. C., “Statistische Theorie nichthomogener Turbulenz,” *Zeitschrift fuer Physik*, Vol. 129, 1951, pp. 547–572.

[24] Jones, W. P., and Launder, B. E., “The Prediction of Laminarization with a Two-Equation Model of Turbulence,” *International Journal of Heat and Mass Transfer*, Vol. 15, No. 2, 1971, pp. 301–314.

[25] Castillo, L., Wang, X., and George, W. K., “Separation Criterion for Turbulent Boundary Layers Via Similarity Analysis,” *Journal of Fluids Engineering*, Vol. 126, No. 3, 2004, pp. 297–304.

[26] Thomas, F. O., Putnam, C. M., and Chu, H. C., “On the Mechanism of Unsteady Shock Oscillation in Shock Wave/Turbulent Boundary Layer Interactions,” *Experiments in Fluids*, Vol. 18, Nos. 1–2, 1994, pp. 69–81.

[27] Andreopoulos, J., and Muck, K. C., “Some New Aspects of the Shock-Wave/Boundary-Layer Interaction in Compression-Ramp Flows,” AIAA Paper 1986-342, 1986.

[28] Wu, M., and Martin, M. P., “Direct Numerical Simulation of Shockwave/Turbulent Boundary Layer Interaction,” AIAA Paper 2004-2145, 2004.

[29] Robinson, S. K., “Coherent Motions in the Turbulent Boundary Layer,” *Annual Review of Fluid Mechanics*, Vol. 23, 1991, pp. 601–639.

[30] Ichimiya, M., Nakamura, I., and Yamashita, S., “Properties of a Relaminarizing Turbulent Boundary Layer under a Favorable Pressure Gradient,” *Experimental Thermal and Fluid Science*, Vol. 17, No. 1–2, 1998, pp. 37–48.

C. Bailly
Associate Editor